UNIVERSITY OF
BATH

University of Bath

Electromagnetic Performance Comparison between 12-Phase Switched Flux and Surface-Mounted PM Machines for Direct-Drive Wind Power Generation

Lingyun Shao, Wei Hua*, Juliette Soulard, Z. Q. Zhu, *Fellow*, *IEEE*, Zhongze Wu, Ming Cheng, *Fellow*, *IEEE*

Abstract– In this paper, the 12-phase switched flux (SF) permanent magnet (PM) (SFPM) machine and three surface-mounted PM (SPM) machines designed for direct-drive wind power generation are comparatively analyzed. Firstly, feasible stator-slot/rotor-pole combinations for symmetrical 12-phase winding layout are investigated for both machine topologies. Secondly, the key design parameters of the PM generators including the split ratio and stator teeth width ratio are optimized by finite element (FE) analysis, to achieve a high phase fundamental EMF per turn and a low cogging torque, both of which are desired by the direct-drive wind power generator. Thirdly, electromagnetic performances including air-gap field, cogging torque, static torque, inductance, output voltage and its regulation factor, output power and efficiency of the generators are compared. A 10 kW 24-slot/22-pole SFPM prototype is built and tested to validate the FE predicted results.

Index Terms— Flux switching permanent magnet (FSPM) machine, multi-phase, permanent magnet (PM) machine, surface-mounted permanent magnet (SPM) machine, switched flux permanent magnet (SFPM) machine, wind power generation.

I. INTRODUCTION

DIRECT-DRIVE Permanent Magnet (PM) synchronous generators are attractive for high power wind power applications due to the highest energy yield, compared to the induction generators and electrically excited synchronous generators [1]. Many types of PM wind generators have been proposed, including the conventional rotor-PM generators among which surface-mounted PM (SPM) generators have been commercialized successfully [2] and the stator-PM generators [3].

The switched flux (SF) PM (SFPM) generator [3]-[7] is a typical type of stator-PM generators in which both the PMs and armature windings are located in the stator, leaving the rotor simple and robust. Compared with rotor-PM machines, SFPM machines may have a better thermal dissipation capability since all thermal sources are placed in the stator which is easier for cooling, and hence an improved reliability due to a reduced risk of irreversible demagnetization [8]. Besides, with non-overlapping concentrated coils wound around each stator tooth, SFPM machines can also exhibit a good fault-tolerant capability owing to smaller mutual coupling between different phases than with distributed windings [9].

The multi-phase winding topology reduces the power per phase, allows a reduced power rating for power electronics of each phase, improves the reliability and brings additional degrees of freedom for pre-fault and post-fault operations as well as torque enhancement [10]-[19]. In [20], the multi-phase winding concept was firstly employed in the SFPM machine for aerospace, and the results show that a higher fault-tolerant capability can be achieved with a larger phase number due to a lower mutual inductance. The 5-phase SFPM machine for high reliability applications is designed and analyzed in [21], and a modified design exhibiting lower eddy current loss is proposed in [22] with added rotor flux barriers. In [5], a 9-phase SFPM machine is proposed and analyzed in terms of electromagnetic performance. In [23], a 12-phase SFPM machine is proposed for direct drive PM generators for wind power generation, which exhibits a higher air-gap flux density, a higher torque/power density, and a lower voltage regulation factor than the 9-phase counterpart [24].

Surface-mounted PM (SPM) machines have been well developed for wind power generators in market [2], [25]-[27], and the research has been undertaken to cover both single phase SPM generators [28]-[30] and multi-phase ones [31], as well as the control [32]. A comparison between three-phase SFPM and SPM high speed generators at 12,700 r/min has been given in [4], which focuses on the mechanical design and optimization of the rotors in high-speed SFPM and SPM generators. As for electromagnetic performance, only the torque versus armature MMF and that versus DC copper loss are compared in [4]. Although the 12-phase SFPM generator for direct-drive wind power generation has been reported in [6] and [23], however a comparison with its SPM counterpart in terms of the electromagnetic performance is still missing. This paper aims to fulfil this gap by comparing the electromagnetic

L. Shao was with the School of Electrical Engineering, Southeast University, Nanjing 210096, China. She is now with the Centre for Automotive Engineering, University of Surrey, Guildford GU2 7XH, U.K. (e-mail: shaolingyun1990@gamil.com).

W. Hua and M. Cheng are with School of Electrical Engineering, Southeast University, Nanjing 210096, China (e-mail: huawei1978@seu.edu.cn; mcheng@seu.edu.cn).

J. Soulard is with Warwick Manufacturing Group, The University of Warwick, Coventry CV4 7AL, U.K. (e-mail: j.soulard@warwick.ac.uk).

Z. Q. Zhu is with Department of Electronic and Electrical Engineering, The University of Sheffield, Sheffield S1 4DE, U.K. (e-mail: z.q.zhu@sheffield.ac.uk).

Z. Wu is with the Institute for Advanced Automotive Propulsion Systems (IAAPS), Department of Mechanical Engineering, University of Bath, Bath BA2 7AY, U.K. (e-mail: z.wu@bath.ac.uk).

performance between the low-speed 12-phase SFPM generator and its SPM counterpart in terms of air-gap field, cogging torque, static torque, inductance, output voltage and its regulation factor, output power and efficiency, based on a few particular study cases with pure resistive loads. The 12-phase winding topology can be divided into 4 sets of 3-phase windings, which means the computing burden of the fault tolerant control to adjust current vectors in 3-phase machines can be relieved by switching off the whole set of 3-phase windings in which fault occurs. For example, the whole set 1 can be switched off if A1-phase winding is open-circuited, and the generator can still supply ~3/4 of the electric power under healthy condition. Moreover, the 4×3-phase topology may also benefit the system efficiency by actively switching off one or more set of 3-phase windings when the operating power is lower than the rated one. For example, if the rated power of the 4×3-phase generator is P_N whilst the operating power is $0.5P_N$, sets 1 and 2 can be switched off to reduce the power modules switching losses and hence improve the system efficiency possibly. The 12-phase SFPM generator (see Fig. 1(a)) and three 12-phase SPM generators (see Figs. 1(b), (c) and (d)) are designed under the same specifications for direct-drive wind power application.

This paper is organized as follows. In section II, the stator-slot/rotor-pole combinations, key dimensional parameters and number of turns per coil are identified, aiming at high phase EMF, low cogging torque and low voltage regulation factor for each generator type. In section III, electromagnetic performances including both open-circuit and on-load generating characteristics are compared by using 2-D finite element (FE) analysis. In section IV, the steady-state thermal performance of the four generators are compared. In section V, the 12-phase 24-slot/22-pole SFPM prototype is built and tested to verify the FE results.

(a) 24-slot/22-pole SFPM

(b) 24-slot/22-pole-pair SPM

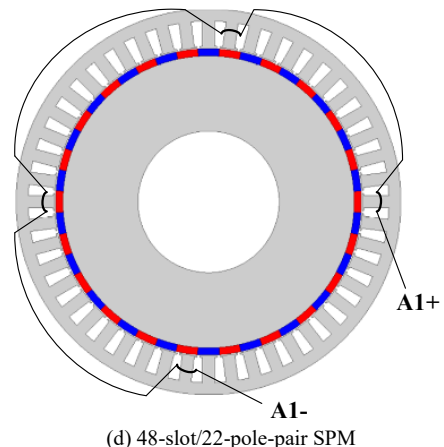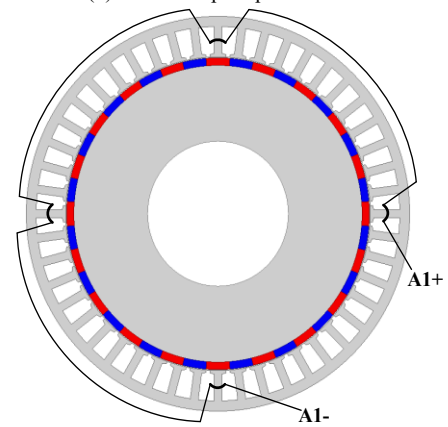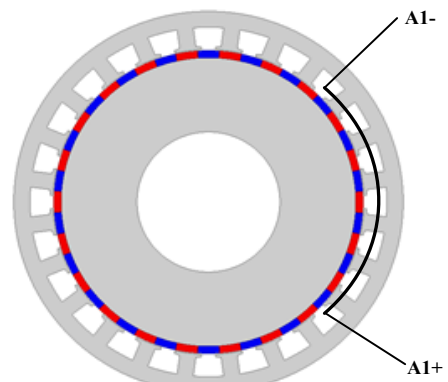(c) 48-slot/20-pole-pair SPM

(d) 48-slot/22-pole-pair SPM
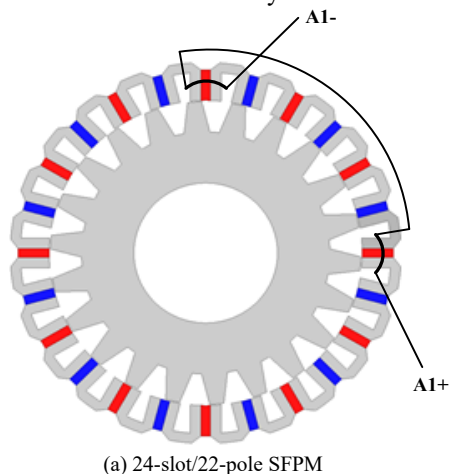
Fig. 1.   Cross-sections of 12-phase PM generators with different topologies.

II. DESIGN PROCESS

The relationship between the tip speed ratio λ, angular velocity ω_r, tip radius R_{tip} and the wind speed v_{wind} of a wind turbine is given in (1). A single blade wind wheel with a radius of R_{tip}=3 m can achieve an optimal tip speed ratio of λ=12, [33], [34], which enables the direct-drive generator to obtain a rated speed of n≈500 r/min at a rated wind speed of v_{wind}=13 m/s. The generators are designed under the same specifications with a rated output power of 10 kW at a rated speed of 500 r/min, which have the same power rating as the TUGE10 direct drive PM generator [35] and the TL-10KW one [36]. The design guidelines and optimization goals are set identical for all generators to make a fair comparison, which has been reported for the 12-phase 24-slot/22-pole SFPM generator in [23].

$$\lambda = \frac{\omega_r R_{tip}}{v_{wind}} \qquad (1)$$

A. Stator-Slot / Rotor-Pole Combination

The stator-slot and rotor-pole numbers are essential for an electrical machine. By choosing appropriate combinations and designing the winding layouts properly, 3rd-order harmonics and even-order harmonics can be eliminated, resulting in a symmetrical phase electromotive-force (EMF) with low harmonic distortion.

The coil-EMFs of the SFPM machines suffer from even-order harmonics, which is caused by the modulation of the rotor permeance's even-order harmonics [37]-[40]. To achieve a symmetrical phase EMF, coils with opposite even-order EMF harmonics are connected in one phase. A null even-order harmonic distribution factor is obtained when the stator-slot number N_s and the phase number m satisfy

$$N_s = 2km \qquad (2)$$

where k=1,2,3… To ease the manufacture of the 12-phase SFPM generator, N_s is designed as the smallest feasible value shown in (2), i.e. N_s=24. A higher number of stator slots would require a shorter air-gap length to prevent the leakage flux between adjacent stator teeth, which would increase the manufacturing difficulties.

As for the rotor-pole number N_r, an even value close to the stator-slot number is desirable for a high pitch factor and avoiding the unbalanced magnetic pull. Here, N_r is selected as 22 to achieve the lower possible electric frequency considering the converter losses.

The topology of the 24-slot/22-pole SFPM generator is shown in Fig. 1(a) where the coil connection of phase A1 is marked. Each phase winding consists of two concentrated coils with "one tooth-one coil" configuration. The open-circuit EMF phasors of the 24 coils are given in Fig. 2(a), and a symmetrical 12-phase winding layout can be achieved.

For the 12-phase SPM generator, three stator-slot and rotor-pole combinations are chosen, i.e. the 24-slot/22-pole-pair one shown in Fig. 1(b), the 48-slot/20-pole-pair one shown in Fig. 1(c), and the 48-slot/22-pole-pair one shown in Fig. 1(d). The first is selected to achieve the same electric frequency and same slot number as the SFPM generator, while the latter two are adopted to achieve the concentrated winding topology with the last one has the same electric frequency as the SFPM generator.

(c) Coil-EMF phasors of 48-slot/20-pole-pair SPM

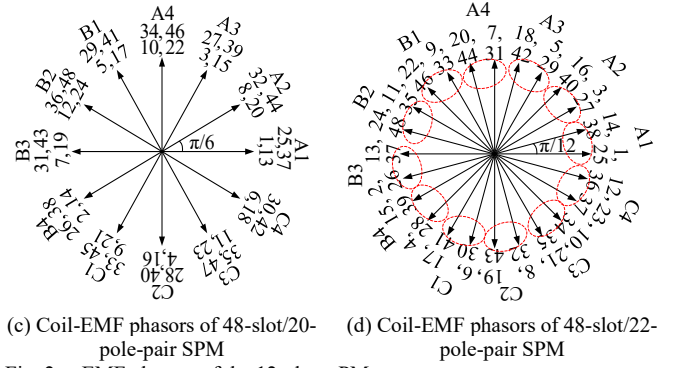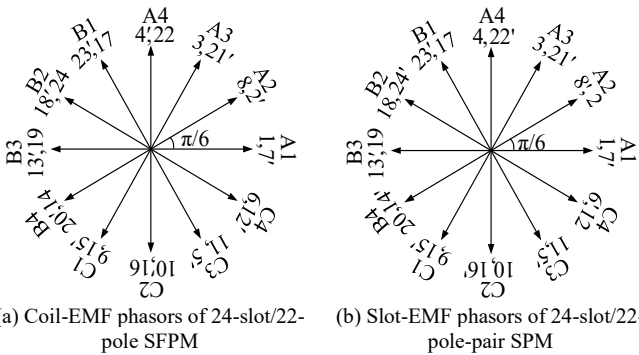(d) Coil-EMF phasors of 48-slot/22-pole-pair SPM

Fig. 2.   EMF phasors of the 12-phase PM generators.

It should be noted that the concentrated winding adopted by the SFPM generator and the 48-slot/20-pole-pair and SPM generator reduces the end-winding length while keeping a high pitch factor k_p equal to cos(15°)=0.966, as shown in Fig. 2(a) and Fig. 2(c). The concentrated winding employed in the 48-slot/22-pole-pair SPM generator shown in Fig. 2(d) can achieve an even higher k_p=cos(7.5°)=0.991. However, k_p is as low as 0.26 when this winding type is used in the 24-slot/22-pole-pair SPM machine. Therefore, overlapping winding is applied on the 24/22-pole-pair SPM machine, as shown in Fig. 1(b), where each phase winding consists of one full pitch coil. The slot-EMF phasors of the 24/22-pole-pair SPM machine are illustrated in Fig. 2(b).

TABLE I
KEY PARAMETERS OF THE SFPM GENERATOR AND SPM GENERATORS

Item	Unit	24/22 SFPM	24/22 SPM	48/20 SPM	48/22 SPM
Stator outer radius, R_{so}	mm	163.5			
Rotor inner radius, R_{ri}	mm	60			
Stack length, L_s	mm	185			
Machine volume, V_{so}	m³	1.55×10^{-2}			
Air-gap thickness, g	mm	1			
Stator yoke radius, R_{sy}	mm	154.94	149.80	155.80	153.2
Stator inner radius, R_{si}	mm	130.8			
Rotor outer radius, R_{ro}	mm	129.8			
Rotor yoke radius, R_{ry}	mm	103.84	123.73	123.73	123.73
Stator tooth width, W_{st}	mm	8.97	13.69	7.70	10.27
Stator slot opening, O_{ss}	mm	8.56	11.41	4.85	2.28
Stator PM width, W_{PM}	mm	7.71	-	-	-
Rotor PM arc, θ_{PM}	°	-	8.18	9	8.18
Rotor pole arc, θ_{rp}	°	5.25	-	-	-
Rotor yoke arc, θ_{ry}	°	12.08	-	-	-
Slot current density, J_{srms}	A/mm²	2.5			
Total stator slot area, A_s	mm²	6793.97	9961.47	12988.11	8680.21
Number of turns per coil, N_c	-	65	85	40	40
Number of strands per turn, N_{st}	-	2	4	3	2
Slot filling factor, k_{sf}	-	0.60	0.54	0.58	0.58
Conductor copper diameter, d_c	mm	0.912 (AWG19)			
Parallel branch number, b	-	1			
Lamination type	-	DW465-50			
N35 PM remanence at 22 °C, B_r	T	1.18			
N35 PM relative permeability at 22 °C, μ_r	-	1.05			

(a) Coil-EMF phasors of 24-slot/22-pole SFPM

(b) Slot-EMF phasors of 24-slot/22-pole-pair SPM
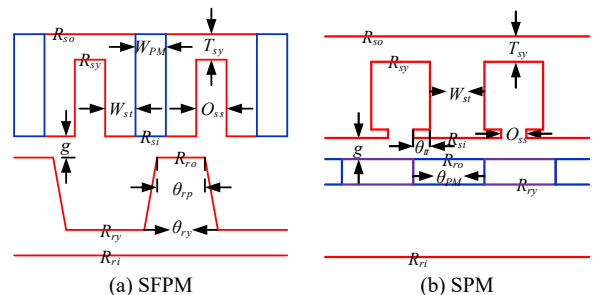

(a) SFPM

(b) SPM

Fig. 3.   Linear illustration of main dimensional parameters.

B. Key Dimensional Parameters

The main dimensional parameters of the generators are defined in Fig. 3. Two key parameters are the split ratio and the stator tooth width ratio for all the four generators, as they are more sensitive to electromagnetic performance than other parameters in both SFPM machines [42] and SPM machines [43]. The split ratio is defined as the ratio of the stator inner radius R_{si} to the stator outer radius R_{so}. The stator tooth width ratio is defined as the ratio of stator tooth width W_{st} to the original tooth width which is 1/4 of the stator slot pitch for the SFPM machine and half of the stator slot pitch for the SPM machines. With a fixed slot current density root mean square (RMS) value J_{srms}=2.5 A/mm^2, they are optimized for a high phase fundamental EMF per turn and a low cogging torque, both of which are desired by the direct-drive wind power generator. During the optimization, the ratio of the stator slot opening to the stator slot pitch is fixed as 1/4 for the SFPM machine [8], [41], whilst in the SPM machine, the tooth tip circumferential arc θ_{tt} is fixed as 2 degrees for the 24-slot/22-pole-pair one and 1 degree for two 48-slot ones. The stator yoke thickness T_{sy} is set equal to the stator tooth width W_{st} for both SFPM and SPM machines, to achieve a similar saturation level in stator yoke and the stator tooth. Moreover, the stator outer diameter, stack length and the air-gap thickness are set equal for a fair comparison. The PM volume of the three SPM generators is set as the same as the SFPM generator design, which has been reported in [23]. It is worth noting that the optimization here is not exhaustive, a global optimization could be conducted to achieve more possible best designs.
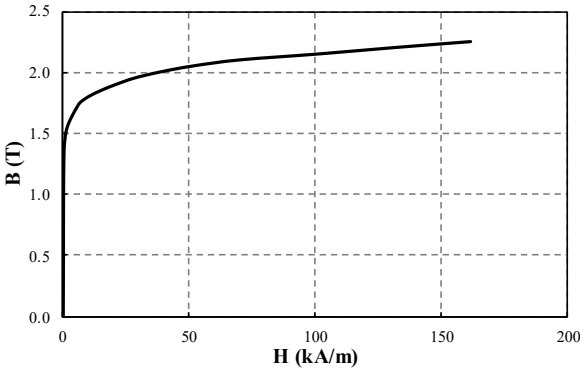

Fig. 4.   B-H curve of DW465-50 lamination.

Based on the lamination B-H curve shown in Fig. 4 and the magnet properties shown in TABLE I, the performance curves versus split ratio and stator tooth width are shown in Fig. 5 to Fig. 8, respectively. Tradeoffs have to be made between the optimization goals, i.e. highest open-circuit phase EMF per turn and lowest cogging torque. They cannot be obtained at the same time. As shown in Fig. 5 to Fig. 8, the optimal points marked "optimal" in the optimization curves of split ratio and stator tooth width ratio are selected to achieve the highest fundamental EMF value per turn with a reasonable peak cogging torque.
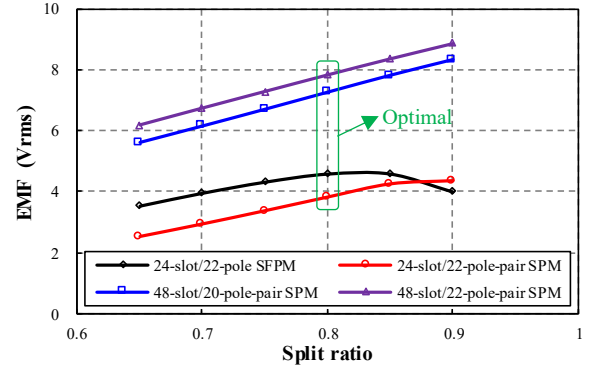

Fig. 5.   Influence of split ratio on phase EMF RMS value (1 turn).
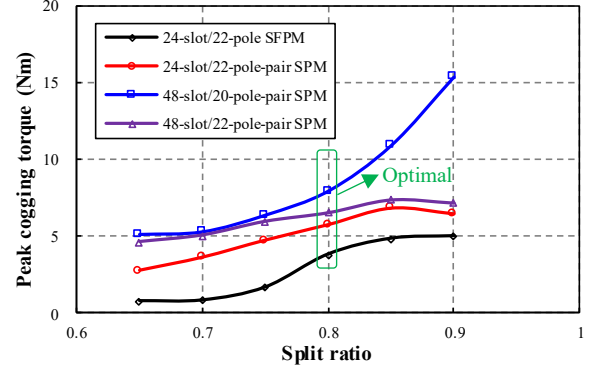

Fig. 6.   Influence of split ratio on peak value of cogging torque.
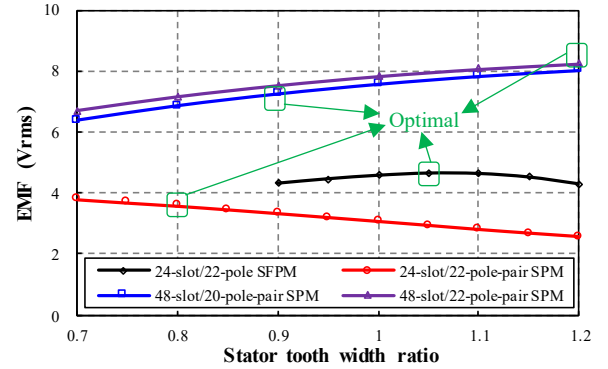
Fig. 7.   Influence of stator tooth width on phase EMF RMS value (1 turn).
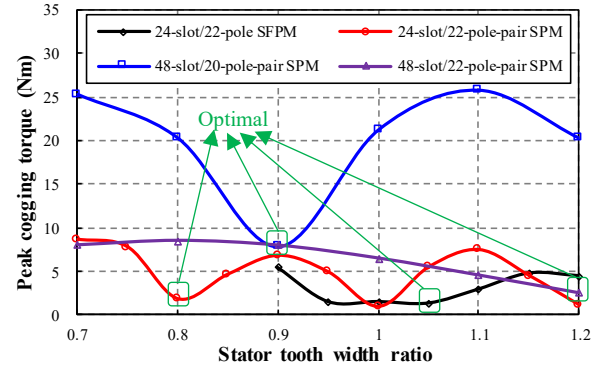
Fig. 8.   Influence of stator tooth width on peak value of cogging torque.

C. Number of Turns per Coil

The number of turns per coil N_c should be designed carefully not only to meet the demand of rated output voltage of a RMS value of 220 V per phase at rated condition, but also to keep a low voltage regulation factor.

The voltage regulation factor ΔU is calculated by

$$\Delta U = \left(\frac{E_0}{U_o} - 1 \right) \times 100\% \qquad (3)$$

where E_0 and U_o are the open-circuit phase EMF and output voltage at the rated speed, respectively.

When the generators operate with a pure resistive load,

the phase current I_o will be in phase with the output voltage U_o. The corresponding phasor diagram of the generators are shown in Fig. 9, where R_{ph} and X_s are the winding resistance and synchronous reactance of each phase, respectively. β is the load angle, which is defined as the phase angle by which phase current I_o lags behind open-circuit phase EMF E_0. According to the phasor diagram, equation (4) can be obtained:

$$E_0 = I_o \sqrt{\left(R_N + R_{ph}\right)^2 + X_s^2} \qquad (4)$$

where R_N is the external resistive load, i.e. $U_o = I_o R_N$.

Then the expression of voltage regulation factor ΔU can be written as,

$$\Delta U = \left(\frac{\sqrt{\left(R_N + R_{ph}\right)^2 + X_s^2}}{R_N} - 1\right) \times 100\% \qquad (5)$$

As shown in (5), the voltage regulation factor increases with the number of turns per coil N_c, since the winding resistance R_{ph} is proportional to N_c and the reactance X_s is proportional to the square of N_c.
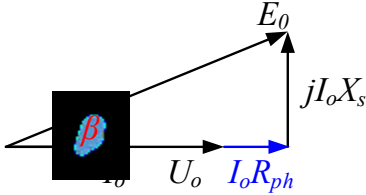

Fig. 9.   Simplified voltage phasor of a generator with a pure resistive load.

The influence of the number of turns per coil N_c on the output power and voltage regulation factor for the generators operating with the rated resistive load R_N at 500 r/min are predicted, as shown in Fig. 10. It can be learned from Fig. 10(b) that a higher number of coil turns is not always beneficial for a higher output power, since the voltage regulation factor gets worse quickly, which may cause a decrease of the output voltage and hence the power. Therefore, the number of turns per coil cannot be too high. It should be optimized to achieve a high power but a low voltage regulation factor. By considering the voltage or power decrement caused by stacking factor and end-effect, N_c is designed as 65 for the SFPM generator, whilst $N_c=85$ for the 24-slot/22-pole-pair, $N_c=40$ for the 48-slot/20-pole-pair, and $N_c=40$ for the 48/22-pole-pair SPM generators, respectively, as shown in TABLE I. It also reveals that the design of the 24-slot/22-pole-pair SPM generator cannot match the rated specification of 10 kW output power due to the restriction of the stator/rotor-pole combination, as shown in Fig. 10(b).

Considering a slot filling factor $k_{sf}=0.6$ can be achieved, the AWG19 copper wire is selected for the 24-slot/22-pole SFPM design with a number of strands per coil $k_{st}=2$, as show in TABLE I. Slightly lower slot filling factors can be achieved in the 24-slot/22-pole-pair, 48-slot/20-pole-pair SPM and 48-slot/22-pole-pair SPM generators, i.e. 0.54, 0.58 and 0.58, respectively, as shown in TABLE I.

(a) 24-slot/22-pole SFPM

(b) 24-slot/22-pole-pair SPM

(c) 48-slot/20-pole-pair SPM

(d) 48-slot/22-pole-pair SPM
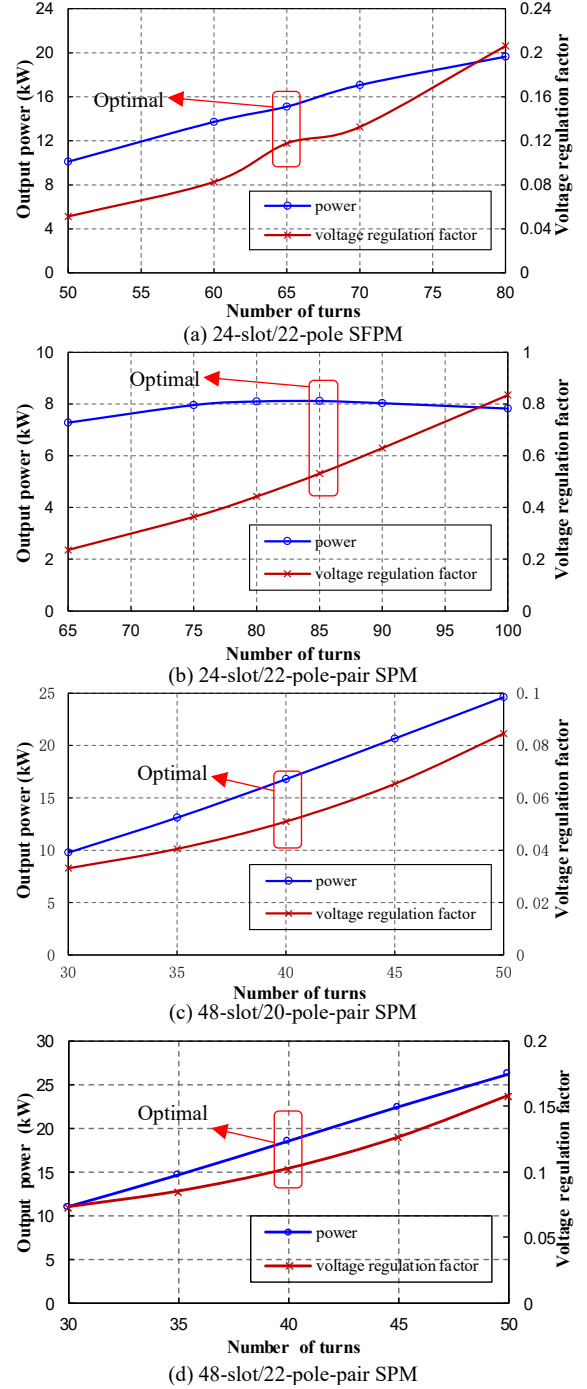
Fig. 10.   Influence of number of turns per coil on the on-load output power and voltage regulation factor with a rated resistive load $R_N=58\ \Omega$.

III.   COMPARISON OF ELECTROMAGNETIC PERFORMANCE

After the optimization, the electromagnetic performances including open-circuit static characteristics and on-load generating performances of the generators are predicted and compared basing on 2-D FE analysis.

A.   Open-Circuit Characteristics

As shown in Fig. 11, the SFPM machine has a more sinusoidal phase EMF than the SPM counterparts, although it has stronger air-gap field harmonics (see Fig. 12). This is explained as follows.

(a) Waveforms

(b) Spectra
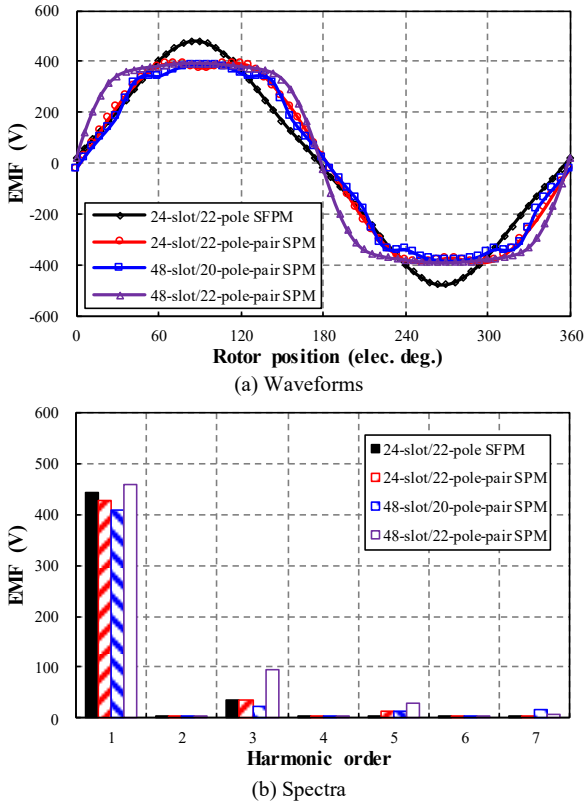
Fig. 11. Open-circuit phase EMF at 500 r/min.

(a) Waveforms

(b) Spectra
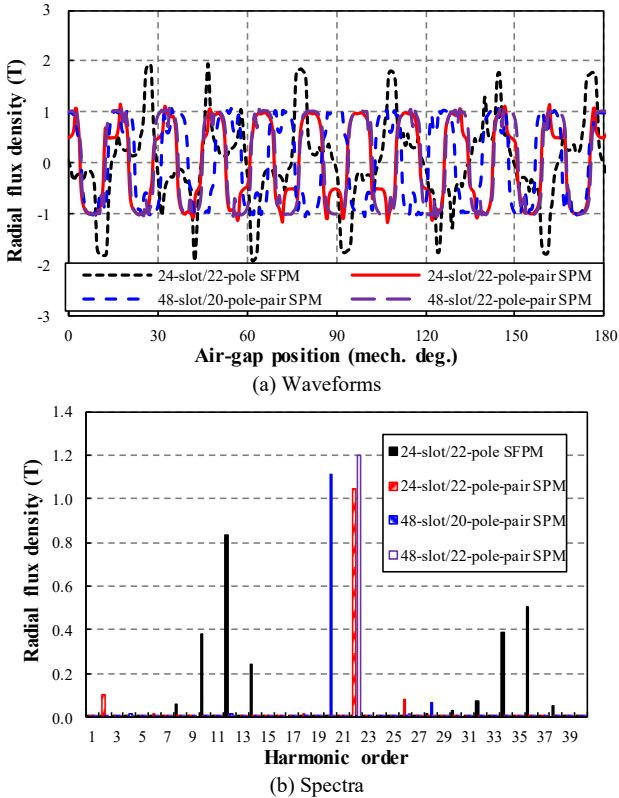
Fig. 12. Open-circuit air-gap radial flux density.

The harmonic air-gap fields play a leading role. The reason lies in the modulation effect of the salient rotor in the SFPM machines [37]-[40], which makes the air-gap field harmonics produced by PM and armature reaction rotate synchronously to generate electromagnetic torque. The air-gap flux density for the SFPM machine is apparently higher than the SPM counterparts due to flux-focusing effect. The phase fundamental EMF magnitude for the 48-slot/22-pole-pair and 48-slot/20-pole-pair SPM generators have the highest and lowest values, respectively. As shown in Fig. 11(b) and TABLE II, the 48-slot/22-pole-pair SPM generator exhibits a 3.9% higher phase fundamental EMF than the SFPM one.

As shown in Fig. 11(b) and TABLE II, the 24-slot/22-pole SFPM generator also features a lower harmonic content and hence the smallest total harmonic distortion (THD) for the phase EMF waveform, due to the cancellation of even-order harmonics of coils belong to the same phase, i.e. zero distribution factor for even-order harmonics, and also the low pitch factor for other harmonics [44]. Here, THD of the phase EMF waveform is defined as,

$$THD = \frac{\sqrt{E_2^2 + E_3^2 + E_4^2 + \cdots}}{E_1} \qquad (6)$$

where E_1 is the phase EMF fundamental value, whilst E_k (k=2,3,4,…) is the kth harmonic amplitude.

The cogging torque of all three SPM generators are larger than that of the SFPM generator but in the similar level, as shown in Fig. 13(a). The cogging torque harmonics of three SPM generators and the SFPM generator are comparatively shown in Fig. 13(b). As shown in Fig. 13(b), the cogging torque harmonic orders of each SPM generators having stator slot number Q and pole-pair number p are integer multiple of $LCM(Q,2p)/p$ [45], where LCM is the least common multiplier, although the 12th cogging torque harmonic in the 48-slot/20-pole-pair SPM generator is small. Similarly, the cogging torque harmonic orders in the 24-slot/22-pole SFPM generator are integer multiple of $LCM(24,22)/22=12$.

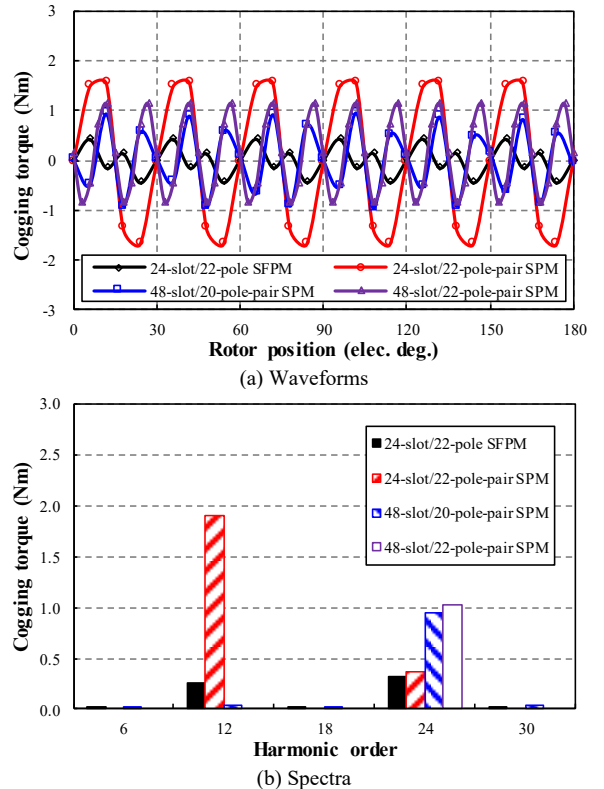

(a) Waveforms

(b) Spectra

Fig. 13. Cogging torques.

B. On-Load Generating Performances

The on-load performances including output voltage and power, torque, voltage regulation factor and efficiency of the SFPM and SPM generators working at 500 r/min with 12-phase resistive loads have been simulated.
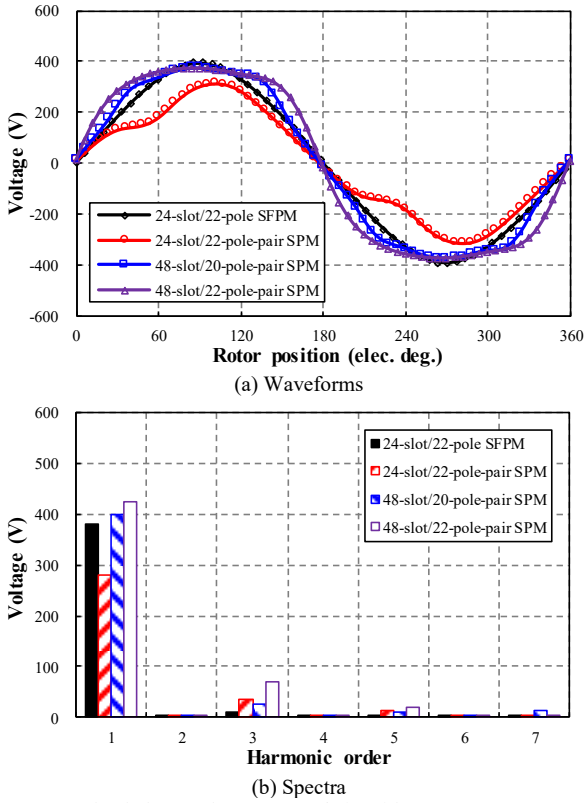
(a) Waveforms

(b) Spectra

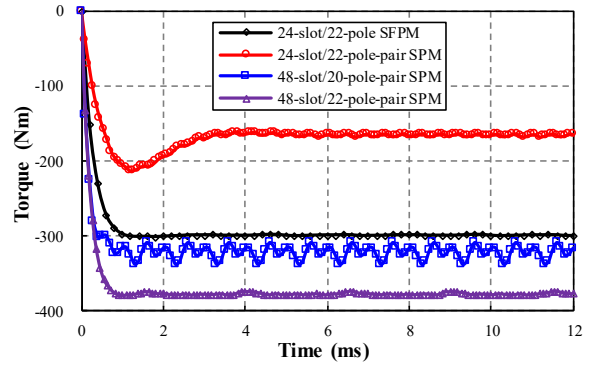Fig. 14.   On-load phase voltage at 500 r/min with R_N=58 Ω.

Fig. 15.   On-load electromagnetic torque waveforms at 500 r/min with R_N.
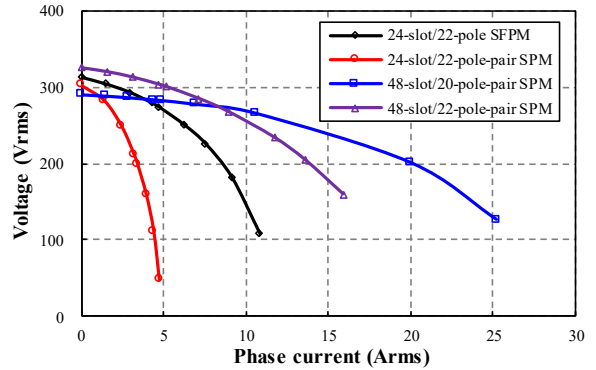

Fig. 16.   Influence of on-load phase fundamental RMS current on output voltage within a resistive load range at 500 r/min.
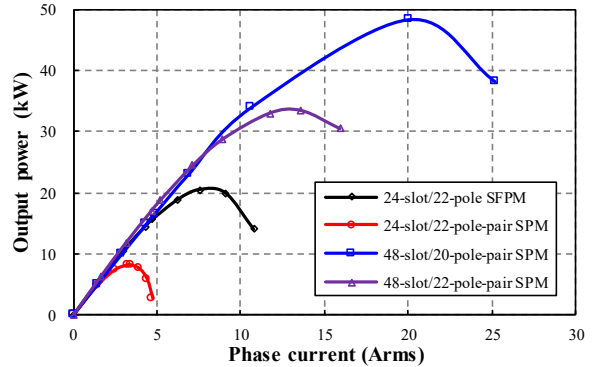

Fig. 17.   Influence of on-load phase fundamental RMS current on output power within a resistive load range at 500 r/min.

The output voltage waveforms at rated generating condition with the rated resistive load R_N=58 Ω are shown in Fig. 14. According to the harmonic analysis results shown in Fig. 14(b), the 48-slot/22-pole-pair SPM generator has the highest fundamental output voltage magnitude, whilst the 24-slot/22-pole-pair SPM generator exhibits the lowest one, although their open-circuit phase EMFs are closer (see Fig. 11). This phenomenon indicates that the voltage regulation factor for the 24-slot/22-pole-pair SPM generator is much larger. The feature values are calculated in TABLE II. The root cause of the difference lies in the inductance values. The 24-slot/22-pole-pair SPM generator has a particularly higher inductance, which causes a larger load angle β as shown in TABLE II. This brings a worse voltage regulation factor, since ΔU is positively correlated with $1/\cos\beta$ when the winding resistance R_{ph} is neglected, and a lower electromagnetic torque as shown in Fig. 15. The small overshoot on the torque waveform of the 24-slot/22-pole-pair SPM generator is caused by the high winding inductance as shown in TABLE II. As shown in Fig. 14(b) and TABLE II, similar to the trend for THD of the open-circuit phase EMF, the 24-slot/22-pole SFPM generator also exhibits a lower THD of the on-load phase voltage than the three analyzed SPM generators.

The lowest THD of the on-load phase voltage shown in Fig. 14(b) and the lowest cogging torque shown in Fig. 13 also contribute the smallest torque ripple of the 24-slot/22-pole SFPM generator, as shown in Fig. 15 and TABLE II. The torque ripple T_{rip} in TABLE II is defined as,

$$T_{rip} = \frac{T_{max} - T_{min}}{T_{ave}} \times 100\% \qquad (7)$$

where T_{max}, T_{min} and T_{ave} are the maximum, minimum and average torque values.

The generating performance of the four generators operated within a resistive load range at 500 r/min are analyzed as shown in Fig. 16 to Fig. 18. The stability of the output voltage when the external load changes can be reflected by the slopes of the curves in Fig. 16. Clearly, the output voltage for the 48-slot/20-pole-pair SPM generator can be kept more stable than the other three when the load current changes slightly from the rated point. From Fig. 17, the overload capability of the generators can be evaluated by the peak point and rated point of the curves. The maximum powers of the 48-slot/20-pole-pair SPM, the 48-slot/22-pole-pair SPM and SFPM generator are about 2.9, 1.78 and 1.35 times of the rated values, respectively. The peak point is very close to the rated point in 24-slot/22-pole-pair SPM machine. This is again due to the largest inductance shown in TABLE II. The efficiency curves in Fig. 18 also shows that the 48-slot/20-pole-pair SPM generator can efficiently operate within a wide load range. In this paper, the efficiency η of the generator is given by,

$$\eta = \frac{P_o}{P_i} \times 100\% = \frac{P_{EM} - p_{cu}}{P_{EM} + p_{fe} + p_{PM}} \times 100\% \qquad (8)$$

where P_o and P_i are the output electric power and the input

mechanical power, respectively. P_{EM} is the electromagnetic power. p_{cu}, p_{fe} and p_{PM} are the copper loss, iron loss and PM eddy current loss, respectively.

The iron loss p_{fe} shown in TABLE II consists of three parts [46] including the hysteresis loss p_{hy}, the eddy current loss p_{ed} and the excess loss p_{ex},

$$p_{fe} = p_{hy} + p_{ed} + p_{ex}$$
$$= k_{hy}fB_m^2 + k_{ed}f^2B_m^2 + k_{ex}f^{1.5}B_m^{1.5} \tag{9}$$

where k_{hy}, k_{ed} and k_{ex} are the loss coefficients for the hysteresis loss, eddy current loss and excess loss, respectively. Here, the hysteresis loss coefficient and the eddy current loss coefficient of the lamination DW465-50 are set as k_{hy}=168 W/m³ and k_{ed}=0.822 W/m³, whilst the excess loss coefficient is neglected as k_{ex}=0. B_m is the maximum flux density.

The PM eddy current loss p_{PM} shown in TABLE II is the sum of each magnet eddy current loss, which is given by,

$$p_{PM} = \frac{1}{\sigma} \int J^2 \, dV \tag{10}$$

where σ is the PM conductivity, which is 6.25×10^5 s/m. J is the eddy current. V is the corresponding volume for each magnet.
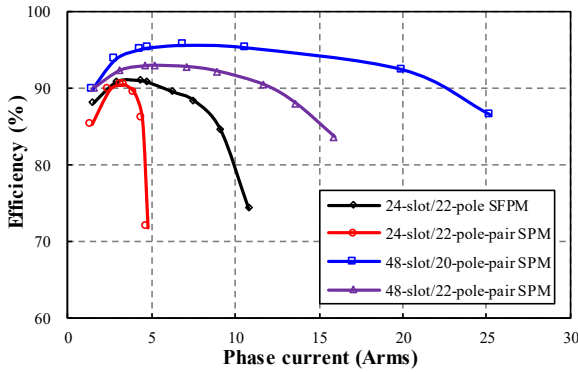

Fig. 18. Influence of on-load phase fundamental RMS current on efficiency within a resistive load range at 500 r/min.

TABLE II
2-D FE-PREDICTED CHARACTERISTICS OF FOUR ANALYSED GENERATORS
(TEMPERATURE: 22 ℃)

Item	Unit	24/22 SFPM	24/22 SPM	48/20 SPM	48/22 SPM
E_o (RMS)	V	313.6	303.1	290	325.8
THD of phase EMF E_o	%	7.9	9.1	8.6	21.5
Rated U_o (RMS)	V	274.4	198.9	282.5	300.9
Rated I_o (RMS)	A	4.73	3.43	4.87	5.19
THD of phase voltage U_o	%	3.8	14.5	7.8	16.7
Rated output power, P_o	kW	15.6	8.2	16.5	18.7
Rated torque, T_e	Nm	-312.8	-165.2	-322.5	-377.7
Torque ripple, T_{rip}	%	0.6	3.7	9	1.4
Voltage regulation factor	%	12.3	52.4	2.7	8.3
Self-inductance, L_{A1A1}	mH	11.8	30.1	5.1	7.9
Load angle, β	°	20	42	8.3	13
Copper loss, p_{cu}	W	443.3	91.7	170.8	581.5
Iron loss, p_{fe}	W	322.4	171.4	368.8	348.3
PM loss, p_{PM}	W	104.7	222.3	71.4	32.9
Total loss, p_{total}	W	870.4	485.4	611.0	962.7
Efficiency, η	%	94.8	94.6	96.5	95.2

IV. STEADY-STATE THERMAL PERFORMANCE

In the foregoing analysis, the temperature of all generator components including winding and PM are set as 22 ℃. However, as well known, a different temperature will influence the PM characteristics and winding resistance, and hence the electromagnetic performance listed in TABLE II. In this section, the steady-state thermal performance of all the four analyzed generators are analyzed and given as follows.

A. Convective Heat Transfer Coefficient between Housing and Ambient

In [47], the thermal performance of a 9-phase SFPM generator [5] with axial fins on housing is analyzed, which has the same stator outer radius R_{so} as the four analyzed generators in this paper. By employing the housing with axial fins of the 9-phase SFPM generator in [48] to the four analyzed generators here, the convective heat transfer coefficient between housing and ambient h_h can be given by [47], [48],

$$h_h = \frac{\rho_{air}c_{air}Dv}{4L_f}(1 - e^{-m_h}) \tag{11}$$

where ρ_{air} and c_{air} are the mass density and the specific heat capacity of air, respectively. D is the hydraulic diameter in unit of meter. v is the inlet air velocity in the fin channels. L_f is the axial length of cooling fins. m_h is given by [48],

$$m_h = \frac{0.1448 \times L_f^{0.946}}{D^{1.16}} \times \left(\frac{k_{air}}{\rho_{air}c_{air}v}\right)^{0.214} \tag{12}$$

where k_{air} is the air thermal conductivity.

Based on (11) and (12), when the generator is operating at 500 r/min, the convective heat transfer coefficient between housing and ambient for all the four analyzed generators can be calculated as h_h=137 W/m²/℃ [47].

B. Air-Gap Convective Heat Transfer Coefficient

The Taylor number Ta_g based on mean air-gap radius is given by (13), where Ω_r is the rotating speed of the rotor in unit of rad/s, R_g is the air-gap radius, i.e. R_g=(R_{si}+R_{ro})/2, v_{air} is the air fluid kinematic viscosity [49]. Based on (13), the Taylor number of the air-gap can be calculated as Ta_g=31.62, which is smaller than the critical Taylor number $Ta_{g,cr}$=41.19. Hence, the flow remains a Couette flow [49].

$$Ta_g = \frac{\Omega_r R_g^{0.5}(R_{si} - R_{ro})^{1.5}}{v_{air}} \tag{13}$$

The geometry factor of the air-gap F_g is given by (14), where S is given in (15) [49]. Based on (14) and (15), the geometry factor of the air-gap can be calculated as $F_g \approx 1$.

$$F_g = \frac{\pi^2}{41.19\sqrt{S}}\left(1 - \frac{R_{si} - R_{ro}}{2R_g}\right)^{-1} \tag{14}$$

$$S = 0.0571\left(1 - 0.652\frac{(R_{si} - R_{ro})/R_g}{1 - (R_{si} - R_{ro})/2R_g}\right)$$
$$+ 0.00056\left(1 - 0.652\frac{(R_{si} - R_{ro})/R_g}{1 - (R_{si} - R_{ro})/2R_g}\right)^{-1} \tag{15}$$

As $Ta_g^2/F_g^2 < 1700$, the heat transfer is dominated by conduction and the Nusselt number of the air-gap Nu_g can be given by (16) [49]. Based on (16), the Nusselt number can be calculated as $Nu_g \approx 2$. Then, the air-gap convective heat transfer coefficient can be calculated as $h_g \approx 26.1$ W/m²/℃ for all the four analyzed generators, based on (17).

$$\mathrm{Nu}_g = \frac{2[(R_{si} - R_{ro})/R_{ro}]}{\ln[1 + (R_{si} - R_{ro})/R_{ro}]} \tag{16}$$

$$h_g = k_{air} \frac{\mathrm{Nu}_g}{2g} \tag{17}$$

C. Steady-State Thermal Analysis

Based on the calculated convective heat transfer coefficient between housing and ambient h_h=137 W/m²/°C and that for the air-gap $h_g \approx 26.1$ W/m²/°C, the steady-state temperature distribution of the four analyzed generators at 500 r/min with a pure resistive load R_N=58 Ω are shown in Fig. 19. The steady-state winding temperature and magnet temperature are comparatively listed in TABLE III. Here, the isotropic thermal conductivity of the air, stator / rotor core, PM, copper winding and aluminum housing are set as k_{air}=0.026 W/m/°C, k_{iron}=40 W/m/°C, k_{PM}=6.16 W/m/°C, k_{cu}=400 W/m/°C and k_{al}=237.5 W/m/°C, respectively. The 0.5mm thick slot liner material is set as NOMEX with a thermal conductivity k_{li}=0.13 W/m/°C. It is worth noting that these thermal results are based on closed-loop co-simulation between electromagnetic analysis and steady-state thermal analysis with a convergence error 0.5°C for both PM temperature and winding temperature. Electromagnetic analysis predicted losses are used to modify the temperature distribution in thermal analysis, whilst thermal analysis predicted results are used to update the PM characteristics in electromagnetic analysis. In the closed-loop co-simulation, the temperature coefficient of the N35 PM remanence B_r is -1.1×10⁻³ °C⁻¹, whilst that of the coercivity H_c is -6×10⁻³ °C⁻¹. The temperature coefficient of resistance for the copper winding is set as 3.8×10⁻³ °C⁻¹.

(a) 24-slot/22-pole SFPM   (b) 24-slot/22-pole-pair SPM
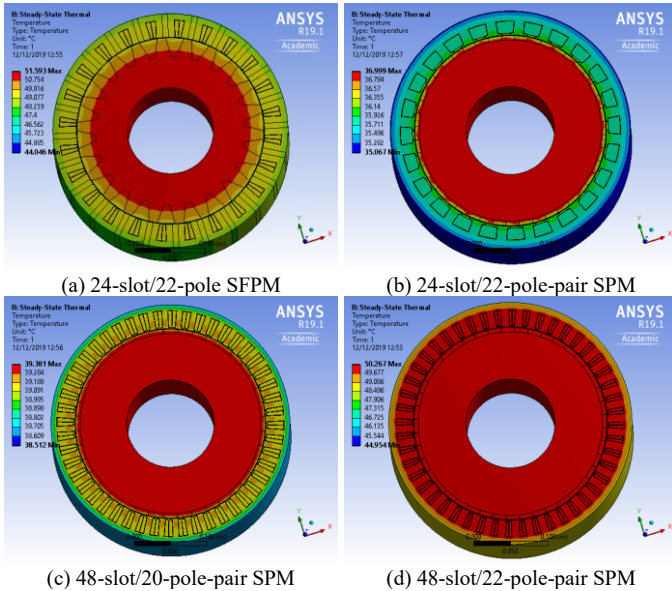
(c) 48-slot/20-pole-pair SPM   (d) 48-slot/22-pole-pair SPM

Fig. 19. Steady-state temperature distribution of four analysed generators at 500 r/min with R_N=58 Ω (housing and shaft not shown).

As shown in Fig. 19 and TABLE III, the SFPM generator and the 48-slot/22-pole-pair SPM generator have a higher winding temperature and PM temperature than the 24-slot/22-pole-pair and 48-slot/20-pole-pair SPM generator, which is mainly due to the larger losses shown in TABLE II. In addition, as listed in TABLE III, the magnet temperature in all the four generators is smaller than the maximum working temperature of N35, i.e. 80 °C.

As shown in TABLE III, by considering the influence of temperature of PM and winding, the average torque of all the four analyzed generators is slightly smaller than their counterparts without consideration of temperature rising listed in TABLE II, i.e. 7.95%, 9.15%, 4.51% and 12.60%, respectively. However, the efficiency is kept similar for all of them.

TABLE III
COMPARISON OF STEADY-STATE PERFORMANCE IN FOUR ANALYSED
GENERATORS AT 500 r/min WITH R_N=58 Ω

Item	Unit	24/22 SFPM	24/22 SPM	48/20 SPM	48/22 SPM
Maximum winding temperature	°C	49.4	35.9	39.2	50.1
Minimum winding temperature	°C	49.2	35.8	39.1	50.0
Average winding temperature	°C	49.4	35.9	39.2	50.1
Maximum PM temperature	°C	49.9	37.0	39.4	50.2
Minimum PM temperature	°C	48.1	36.0	39.1	50.0
Average PM temperature	°C	49.2	36.6	39.3	50.1
Average torque, T_{ave}	Nm	-287.93	-150.08	-307.97	-330.10
Torque ripple, T_{rip}	%	0.5	1.53	4.20	0.89
Copper loss, p_{cu}	W	489.69	96.54	181.95	642.07
Stator iron loss, p_{fe}	W	155.57	159.51	354.49	304.71
Rotor iron loss, p_{fe}	W	149.65	7.92	0.51	0.21
PM loss, p_{PM}	W	168.18	221.41	73.69	36.71
Total loss, ptotal	W	963.09	485.38	610.64	983.70
Efficiency, η	%	96.9	95.2	97.4	98.0

V. EXPERIMENTAL VALIDATION

To validate the previous 2-D FE analysis, the 12-phase 24-slot/22-pole SFPM generator is built and tested, as shown in Fig. 20. The volume and weight of the stator core, rotor core, PMs and copper of the prototype are in TABLE IV. It is worth noting that some of the experimental results have been reported in [6] and [23].

TABLE IV
COMPONENTS VOLUME AND WEIGHT OF THE 24-SLOT/22-POLE SFPM
PROTOTYPE

Item	Unit	Value
Stator core volume	dm³	3.05
Stator core mass density	kg/m³	7850
Stator core weight	kg	24.0
Rotor core volume	dm³	5.81
Rotor core mass density	kg/m³	7850
Rotor core weight	kg	45.6
PMs volume	dm³	0.87
PM mass density	kg/m³	7600
PMs weight	kg	6.6
Copper volume	dm³	0.34
Copper mass density	kg/m³	8933
Copper weight	kg	3.0
Total weight	kg	79.1

A. Open-Circuit

The tested open-circuit phase EMF waveforms for phases A1-A4 of the 12-phase 24-slot/22-pole SFPM prototype at 500 r/min are shown in Fig. 21. As shown in Fig. 22, the measured phase EMF waveform matches well with the 3-D FE predicted result which takes the end leakage flux into account. As shown in Fig. 22(b), the measured phase EMF fundamental amplitude is 7.95% and 4.10% smaller than the 2-D and 3-D FE predicted value, respectively. The measured winding self-inductance and mutual inductance by HIOKI LCR meter also agree well with the 2-D FE predicted values, as shown in Fig. 23.
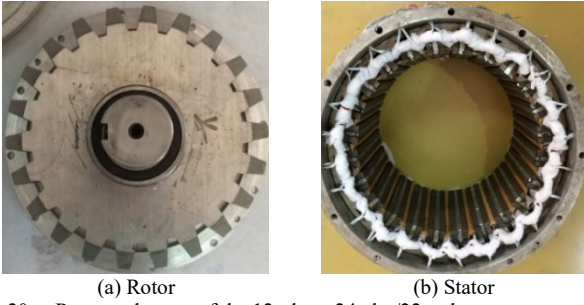
(a) Rotor   (b) Stator

Fig. 20. Rotor and stator of the 12-phase 24-slot/22-pole prototype.
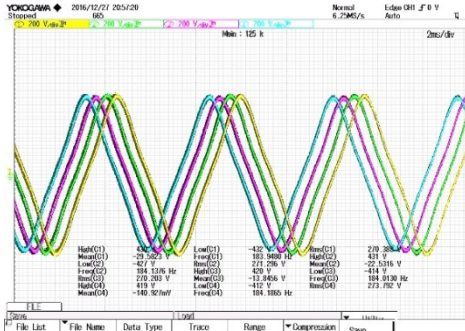

Fig. 21. Tested open-circuit phase EMF waveforms of the 12-phase 24-slot/22-pole SFPM prototype @500 r/min (C1-C4: Phases A1-A4).
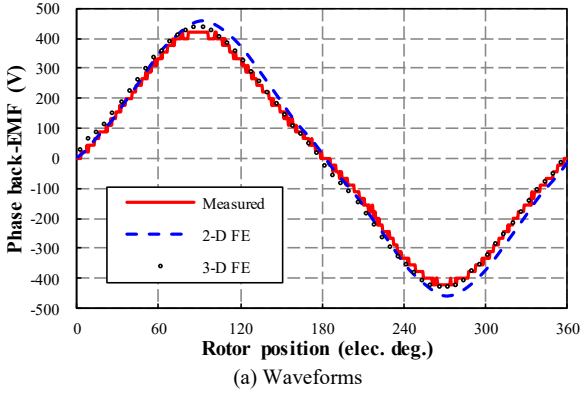

(a) Waveforms

(b) Spectra

Fig. 22. Comparison between the tested and FE predicted open-circuit phase EMF of the 12-phase SFPM prototype @500 r/min.
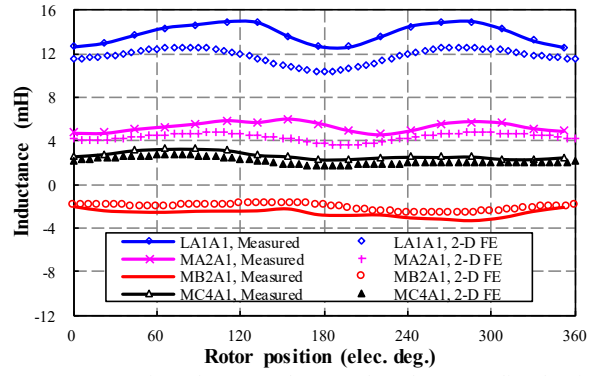

Fig. 23. Comparison between the tested and FE predicted winding inductances of the 12-phase SFPM prototype.

B. Rated On-Load

The test bench for measuring the on-load performances is shown in Fig. 24, including a DC motor to drive the SFPM prototype, a torque sensor to measure the input mechanical torque, and the 12-phase symmetrical pure resistive load (R_N=58 Ω) connected to the SFPM generator's 12-phase windings.
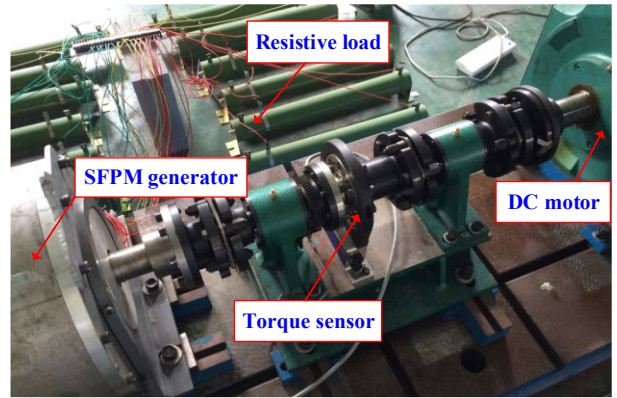

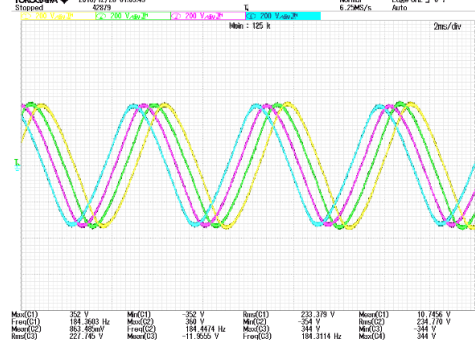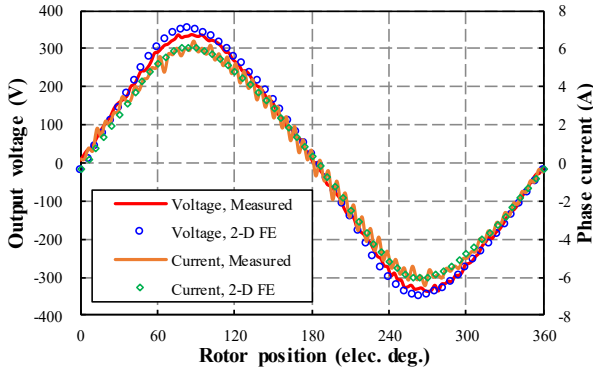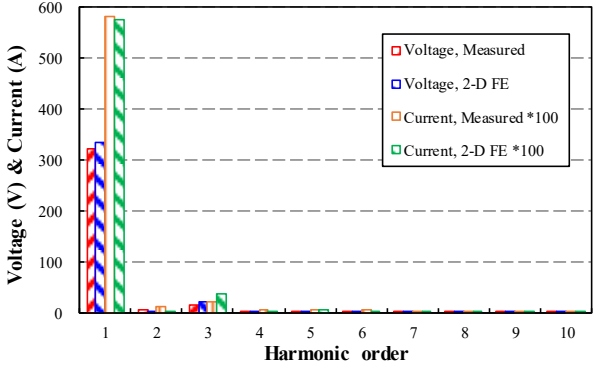Fig. 24. Test bench for SFPM generator with pure resistive load.

Fig. 25. Tested output voltage of the 12-phase 24-slot/22-pole SFPM prototype with resistive load R_N=58Ω @500 r/min (C1-C4: Phases A1-A4).

(a) Waveforms

(b) Spectra

Fig. 26. Comparison between the tested and FE predicted phase winding voltage and current of the 12-phase SFPM prototype with resistive load R_N=58Ω @500 r/min.

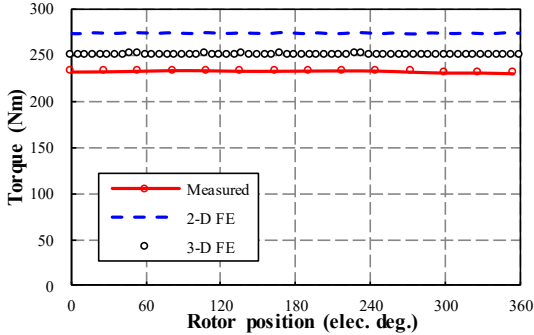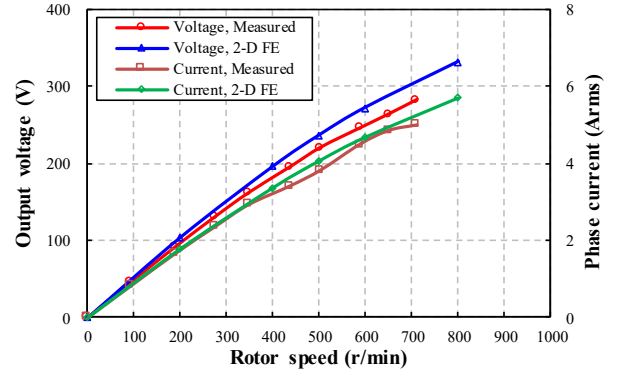Fig. 27. Comparison between the tested mechanical torque and FE-predicted electromagnetic torque (resistive load R_N=58 Ω @500 r/min).

The on-load output voltage for phases A1-A4 of the 12-phase 24-slot/22-pole SFPM prototype at 500 r/min are shown in Fig. 25, which agree well with the 2-D FE predicted value, as shown in Fig. 26 together with the phase winding current in terms of both waveforms and spectra. The measured open-circuit phase fundamental EMF RMS value and the output voltage RMS value are 271 V and 223 V, respectively. Using the test value, the actual voltage regulation factor ΔU and output power P_o can be calculated, as listed in TABLE V. The measured input mechanical torque is shown in Fig. 27, together with the electromagnetic torque predicted by 2-D and 3-D FE analysis. The measured input mechanical torque is 15% lower than the 2-D FE analyzed electromagnetic torque because both the PM flux-linkage and armature current are reduced due to end-effect. After considering the end leakage by using 3-D FE method, the tested torque is 4.8% higher than the predicted value. Finally, the efficiency of the prototype operated at rated power generating condition is obtained through dividing the output power P_o by the input mechanical power P_i which is derived from the measured mechanical torque T_i as shown in

TABLE V. The difference between P_i and P_o comes to the total loss of the generator, including copper loss, iron loss, PM eddy-current loss and mechanical loss.

TABLE V
TEST RESULTS OF THE 24-SLOT/22-POLE SFPM PROTOTYPE AT RATED GENERATOR MODE @500 r/min

Item	Unit	Value
Open-circuit phase fundamental EMF (RMS), E_o	V	271
Output phase voltage (RMS), U_o	V	223
Output phase current (RMS), I_o	A	4
Input mechanical torque, T_i	Nm	224
Input mechanical power, P_i	kW	11.8
Output power, P_o	kW	10.3
Power density, P_o/V_{so}	kW/m³	664.5
Efficiency, η	%	87.8
Voltage regulation factor, ΔU	%	22

(a) Output phase winding voltage and current
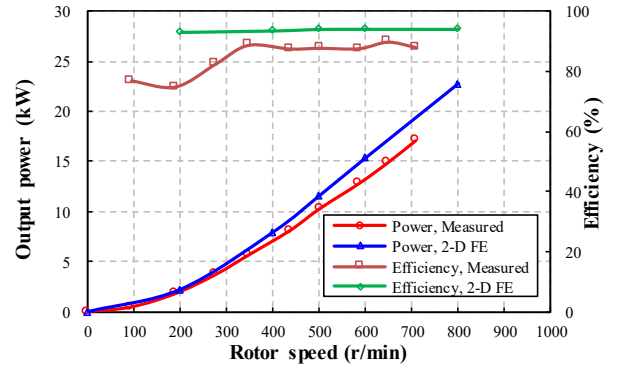
(b) Output electric power and efficiency

Fig. 28. Comparison between the tested output voltage, winding current, power and efficiency at various rotor speeds (resistive load R_N=58 Ω).

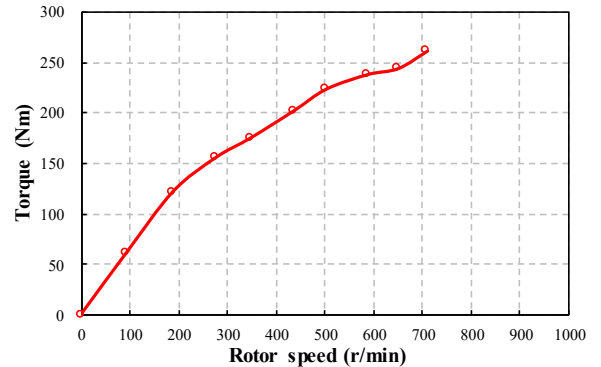Fig. 29. Variation of tested shaft torque with various rotor speeds (resistive load R_N=58 Ω).

C. On-Load with Various Rotor Speeds and Constant Resistive Load R_N=58 Ω

Here the resistive load for each phase winding is fixed as R_N=58Ω to investigate the influence of rotor speed on the output voltage, phase current, output power and efficiency. As shown in Fig. 28, the measured values agree well with

the 2-D FE predicted values at low speeds, however, the difference becomes larger at a high speed. This is due to: i) the severer end flux-leakage caused by more saturated magnetic field [50]; and ii) a higher rotor speed will induce a larger winding current and hence a higher PM temperature within a same time length, which will degrade the PM strength more and hence the output voltage. As shown in Fig. 28(b), the measured efficiencies are lower than those predicted by 2-D FE, due to the neglecting of the eddy current loss of the generator aluminum shell [51], mechanical loss and additional loss.

The lower tested efficiency from 100 r/min to 300 r/min shown in Fig. 28 could be caused by the similar friction torque at different speeds. Since the rolling friction is independent of speed, the friction torque of the ball bearing can be regarded as similar at different speeds. However, the shaft mechanical torque is larger at a higher speed, as shown in Fig. 29. This means the ratio of the friction loss to the shaft mechanical power goes lower at a higher speed. Hence, the efficiency is smaller at low speeds.
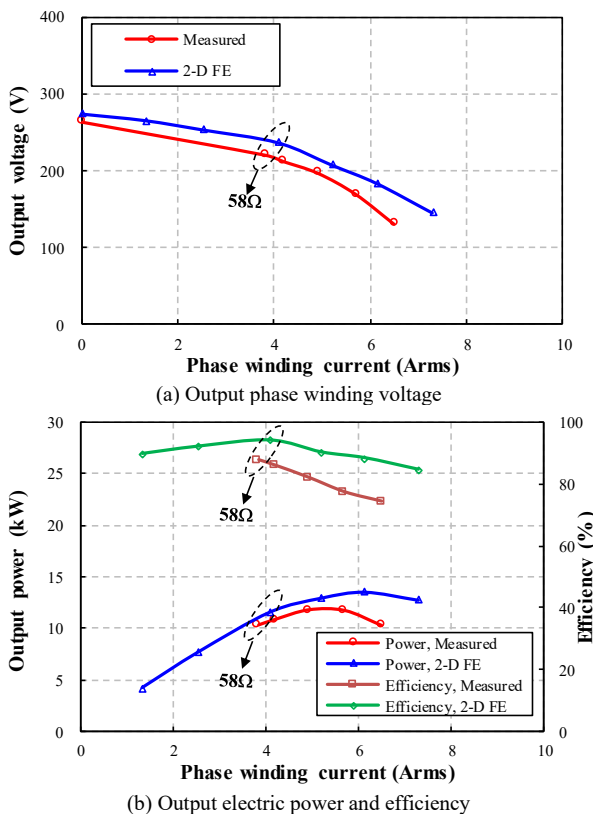

(a) Output phase winding voltage

(b) Output electric power and efficiency

Fig. 30. Comparison between the tested output voltage, power and efficiency versus phase winding current at various resistive loads (rotor speed n_N=500 r/min).

D. On-Load with Various Resistive Loads and Constant Rotor Speed n_N=500 r/min

Here the rotor speed is fixed as n_N=500 r/min, whilst the resistive load for each phase winding is varied with R_N=20 Ω, 30 Ω, 40 Ω, 50 Ω and 58 Ω to investigate the influence of load on the output voltage, phase current and output power. The curves shown in Fig. 30(a) reflect the voltage regulator factor of the prototype, and a higher slope rate stands for a worse voltage regulation. As shown in Fig. 30(a), the measured voltage regulation is worse than that predicted by 2-D FE, due to a higher end flux-leakage caused by a larger load current. It can also be overserved from Fig. 30(b) that the prototype can output the maximum power as ~1.16 times

to the rated value, when the phase resistance is between 30 Ω and 40 Ω.

VI. CONCLUSION

In this paper, the 12-phase SFPM and SPM generators for direct-drive wind power generation are compared in terms of open-circuit and on-load generating performances based on a few particular study cases with pure resistive loads, including the 24-slot/22-pole SFPM generator, 24-slot/22-pole-pair SPM generator, 48-slot/20-pole-pair SPM generator and 48-slot/22-pole-pair SPM generator. It is found that the 48-slot/20-pole-pair SPM generator features a low voltage regulation factor, a high overload capability and a wide operating load range with high efficiency, whilst the 24-slot/22-pole SFPM generator has the lowest cogging torque, torque ripple and voltage harmonics. FE analysis is validated by the experimental results on the SFPM prototype.

As only pure resistance load is considered in this paper and the analysis in this paper is applicable to other load types, future works can be carried out to investigate the influence of load type on these designs and their performances. Also, a global optimization with more dimensional parameters involved could be conducted to obtain better designs for those generators possibly.

REFERENCES

[1] H. Polinder, F. F. A. van der Pijl, G. J. de Vilder, and P. Tavner, "Comparison of direct-drive and geared generator concepts for wind turbines," *IEEE Trans. Energy Convers.*, vol. 21, no. 3, pp. 725–733, Sep. 2006.

[2] Accessed on 25th November 2019. [Online]. Available: https://www.futurenergy.co.uk/generators/

[3] J. Ojeda, M. G. Simoes, G. Li, and M. Gabsi, "Design of a flux-switching electrical generator for wind turbine systems," *IEEE Trans. Ind. Appl.*, vol. 48, no. 6, pp. 1808–1816, Nov./Dec. 2012.

[4] A. S. Thomas, Z. Q. Zhu, and G. W. Jewell, "Comparison of flux switching and surface mounted permanent magnet generators for high-speed applications," *IET Elec. Syst. Transport.*, vol. 1, no. 3, pp. 111–116, Sep. 2011.

[5] F. Li, W. Hua, M. Tong, G. Zhao, and M. Cheng, "Nine-phase flux-switching permanent magnet brushless machine for low-speed and high-torque applications," *IEEE Trans. Magn.*, vol. 51, no. 3, pp. 1–4, Mar. 2015, Art. ID 8700204.

[6] L. Shao, W. Hua, M. Cheng, J. Soulard, Z. Wu and Z. Q. Zhu, "Electromagnetic performance comparison between 12- phase switched flux and surface-mounted PM machines for direct-drive wind power generation," 2018 XIII International Conference on Electrical Machines (ICEM), Alexandroupoli, 2018, pp. 2150–2156.

[7] Y. Wang, and Z. Deng, "Comparison of switched-flux permanent magnet machines with non-overlapping concentrated winding for open-winding generator system," *IET Elec. Power Appl.*, vol. 11, no. 2, pp. 242–251, Feb. 2017.

[8] Z. Q. Zhu, and J. T. Chen, "Advanced flux-switching permanent magnet brushless machines," *IEEE Trans. Magn.*, vol. 46, no. 6, pp. 1447–1453, Jun. 2010.

[9] M. Cheng, W. Hua, J. Zhang, and W. Zhao, "Overview of stator-permanent magnet brushless machines," *IEEE Trans. Ind. Electron.*, vol. 58, no. 11, pp. 5087–5101, Nov. 2011.

[10] E. Levi, "Multiphase electric machines for variable-speed applications," *IEEE Trans. Ind. Electron.*, vol. 55, no. 5, pp. 1893–1909, May 2008.

[11] E. Levi, "Advances in converter control and innovative exploitation of additional degrees of freedom for multiphase machines," *IEEE Trans. Ind. Electron.*, vol. 63, no. 1, pp. 433–448, Jan. 2016.

[12] A. Cavagnino, A. Tenconi, and S. Vaschetto, "Experimental characterization of a belt-driven multiphase induction machine for 48-V automotive applications: losses and temperatures assessments," *IEEE Trans. Ind. Appl.*, vol. 52, no. 2, pp. 1321–1330, Mar.-Apr. 2016.

[13] K. Wang, Z. Y. Gu, Z. Q. Zhu, and C. Liu, "Design and analysis of five phase SPM machine considering third harmonic current injection" *IEEE Trans. Energy Convers.*, vol. 33, no. 3, pp. 1108–1117, Sep. 2018.

[14] K. Wang, Z. Y. Gu, Z. Q. Zhu, and Z. Z. Wu, "Optimum injected harmonics into magnet shape in multi-phase surface-mounted PM machine for maximum output torque," *IEEE Trans. Ind. Electron.*, vol. 64, no. 6, pp. 4434–4443, Jun. 2017.

[15] S. Rubino, R. Bojoi, S. A. Odhano, and P. Zanchetta, "Model predictive direct flux vector control of multi-three-phase induction motor drives," *IEEE Trans. Ind. Appl.*, vol. 54, no. 5, pp. 4394–4404, Sep.-Oct. 2018.

[16] L. Parsa, "On advantage of multiphase machines," in *Proc. of Conf. of IEEE Ind. Electron. Soc.*, Raleigh, USA, pp. 1574–1579, 2005.

[17] S. Brisset, D. Vizireanu, and P. Brochet, "Design and optimization of a nine-phase axial-flux PM synchronous generator with concentrated winding for direct-drive wind turbine," *IEEE Trans. Ind. Appl.*, vol. 44, no. 3, pp. 707–715, May/June 2008.

[18] F. Barrero and M. J. Duran, "Recent advances in the design, modeling and control of multiphase machines—Part I," *IEEE Trans. Ind. Electron.*, vol. 63, no. 1, pp. 449–458, Jan. 2016.

[19] M. J. Duran and F. Barrero, "Recent advances in the design, modeling and control of multiphase machines—Part II," *IEEE Trans. Ind. Electron.*, vol. 63, no. 1, pp. 459–468, Jan. 2016.

[20] A. S. Thomas, Z. Q. Zhu, R. L. Owen, G. W. Jewell, and D. Howe, "Multiphase flux-switching permanent-magnet brushless machine for aerospace application," *IEEE Trans. Ind. Appl.*, vol. 45, no. 6, pp. 1971–1981, Nov./Dec. 2009.

[21] X. Xue, W. Zhao, J. Zhu, G. Liu, X. Zhu, and M. Cheng, "Design of five-phase modular flux-switching permanent-magnet machines for high reliability applications," *IEEE Trans. Magn.*, vol. 49, no. 7, pp. 3941–3944, Jul. 2013.

[22] J. Luo, W. Zhao, J. Ji, J. Zheng, Y. Zhang, Z. Ling, and J. Mao, "Reduction of eddy-current loss in flux-switching permanent-magnet machines using rotor magnetic flux barriers," *IEEE Trans. Magn.*, vol. 53, no. 11, Nov. 2017, Art. ID 17284159.

[23] L. Shao, W. Hua, and M. Cheng, "Design of a twelve-phase flux-switching permanent magnet machine for wind power generation," in *Proc. of Int. Conf. on Elec. Mach. and Syst.*, Hangzhou, China, pp. 435–441, 2014.

[24] L. Shao, W. Hua, F. Li, J. Soulard, Z. Q. Zhu, Z. Wu, and M. Cheng, "A comparative study on nine- and twelve-phase flux-switching permanent-magnet wind generators," in *Proc. of Conf. of IEEE Energy Conversion Congress and Exposition*, Portland, USA, pp. 4283–4289, Sept. 2018.

[25] Accessed on 25th November 2019, Available: https://www.enercon.de/en/products/ep-4/e-141-ep4/

[26] Accessed on 25th November 2019, Available: https://www.ge.com/renewableenergy/wind-energy/offshore-wind/haliade-x-offshore-turbine

[27] Accessed on 25th November 2019, Available: https://www.siemens.com/global/en/home/markets/wind/turbines-and-services

[28] H. Haraguchi, S. Morimoto and M. Sanada, "Suitable design of a PMSG for a large-scale wind power generator," 2009 IEEE Energy Conversion Congress and Exposition, San Jose, CA, 2009, pp. 2447–2452.

[29] G. Madescu, M. Biriescu, M. Greconici, and M. Moţ, "Low speed PM generator for wind turbines applications," 2012 15th International Power Electronics and Motion Control Conference (EPE/PEMC), Novi Sad, 2012, Art. ID DS1c.9.

[30] S. Jia, R. Qu, J. Li, X. Fan, and M. Zhang, "Study of direct-drive permanent-magnet synchronous generators with solid rotor back iron and different windings," *IEEE Trans. Ind. Appl.*, vol. 52, no. 2, pp. 1369–1379, Mar.-Apr. 2016.

[31] A. Damiano, I. Marongiu, A. Monni, and M. Porru, "Design of a 10 MW multi-phase PM synchronous generator for direct-drive wind turbines," IECON 2013 - 39th Annual Conference of the IEEE Industrial Electronics Society, Vienna, 2013, pp. 5266–5270.

[32] M. Morandin, E. Fornasiero, S. Bolognani, and N. Bianchi, "Torque and power rating of a wind-power pm generator drive for maximum profit-to-cost ratio," *IEEE Trans. Ind. Appl.*, vol. 49, no. 2, pp. 866–872, Mar.-Apr. 2013.

[33] http://cdn.intechopen.com/pdfs/16242/InTechWind_turbines_theory_the_betz_equation_and_optima_l_rotor_tip_speed_ratio.pdf, accessed on 20th December 2017.

[34] Z. Zhao, T. Wang, and Y. Zheng, *Theory of Wind Turbines*. Beijing, China: China Water & Power Press, 2016.

[35] https://www.tuge.ee/products/tuge10, accessed on 12th December 2019.

[36] http://wp.china-nengyuan.com/member_product/30161.html, accessed on 20th December 2017.

[37] M. Cheng, P. Han, and W. Hua, "General airgap field modulation theory for electrical machines," *IEEE Trans. Ind. Electron.*, vol. 64, no. 8, pp. 6063–6074, Aug. 2017.

[38] J. D. McFarland, T. M. Jahns, and A. M. EL-Refaie, "Analysis of the torque production mechanism for flux-switching permanent-magnet machines," *IEEE Trans. Ind. Appl.*, vol. 51, no. 4, pp. 3041–3049, July-Aug. 2015.

[39] D. Li, R. Qu, J. Li, W. Xu and L. Wu, "Synthesis of flux switching permanent magnet machines," *IEEE Trans. Energy Convers.*, vol. 31, no. 1, pp. 106–117, Mar. 2016.

[40] Z. Z. Wu and Z. Q. Zhu, "Analysis of air-gap field modulation and magnetic gearing effects in switched flux permanent magnet machines," *IEEE Trans. on Magn.*, vol. 51, no. 5, pp. 1–12, May 2015, Art. ID 8105012.

[41] Z. Q. Zhu, Y. Pang D. Howe, S. Iwasaki, R. Deodhar, and A. Pride, "Analysis of electromagnetic performance of flux-switching PM machines by non-linear adaptive lumped parameter magnetic circuit model," *IEEE Trans. Magn.*, vol. 41, no. 11, pp. 4277–4287, 2005.

[42] Z. Q. Zhu and X. Liu, "Individual and global optimization of switched flux permanent magnet motors," in *Proc. of Inter. Conf. Elec. Mach. and Sys.*, Beijing, China, 2011, pp. 1–6.

[43] W. Q. Chu and Z. Q. Zhu, "Optimal split ratio and torque comparison of surface-mounted permanent magnet machines having inner or outer rotor," in *Proc. of Inter. Conf. Power Electro., Mach. and Dri.*, Bristol, UK, 2012, pp. 1–6.

[44] J. T. Chen and Z. Q. Zhu, "Winding Configurations and Optimal Stator and Rotor Pole Combination of Flux-Switching PM Brushless AC Machines," *IEEE Trans. Energy Convers.*, vol. 25, no. 2, pp. 293–302, Jun. 2010.

[45] N. Bianchi and S. Bolognani, "Design techniques for reducing the cogging torque in surface-mounted PM motors," *IEEE Trans. Ind. Appl.*, vol. 38, no. 5, pp. 1259–1265, Sep.-Oct. 2002.

[46] D. Lin, P. Zhou, W. N. Fu, Z. Badics and Z. J. Cendes, "A dynamic core loss model for soft ferromagnetic and power ferrite materials in transient finite element analysis," *IEEE Trans. on Magn.*, vol. 40, no. 2, pp. 1318–1321, Mar. 2004.

[47] M. Cheng, J. Wang, S. Zhu and W. Wang, "Loss calculation and thermal analysis for nine-phase flux switching permanent magnet machine," *IEEE Trans. Energy Convers.*, vol. 33, no. 4, pp. 2133–2142, Dec. 2018.

[48] D. A. Staton and A. Cavagnino, "Convection heat transfer and flow calculations suitable for analytical modelling of electric machines," IECON 2006 - 32nd Annual Conference on IEEE Industrial Electronics, Paris, 2006, pp. 4841–4846.

[49] D. A. Howey, P. R. N. Childs and A. S. Holmes, "Air-gap convection in rotating electrical machines," *IEEE Trans. Ind. Electron.*, vol. 59, no. 3, pp. 1367–1375, Mar. 2012.

[50] Z. Z. Wu and Z. Q. Zhu, "Comparative analysis of end effect in partitioned stator flux reversal machines having surface-mounted and consequent pole permanent magnets," *IEEE Trans. on Magn.*, vol. 52, no. 7, pp. 1–4, Jul. 2016, Art. ID 8103904.

[51] S. Zhu, M. Cheng, X. Li, and S. Li, "Loss analysis of a new low-speed direct-drive permanent-magnet vernier machine," *Trans. of China Electrotechnical Society*, vol. 30, no. 2, 14–20, Jan. 2015.

Lingyun Shao was born in Jiangsu, China, in 1990. She received the B.Sc. and Ph.D. degrees in electrical engineering from the School of Electrical Engineering, Southeast University, Nanjing, China, in 2012 and 2018, respectively.

Since January 2019, she has been with Centre for Automotive Engineering, Department of Mechanical Engineering Sciences, University of Surrey, Guildford, U. K., where she is currently a research fellow in electric motor simulation and optimization. Her current research interests include the design and analysis of permanent magnet machines for electric propulsion systems and renewable energy generation.

From December 2015 to December 2016, she was also with the Department of Electronic and Electrical Engineering, The University of Sheffield, Sheffield, U.K., as a joint PhD student, sponsored by China Scholarship Council (CSC). From July 2017 to December 2017, she was also with the Warwick Manufacturing Group (WMG), University of Warwick, Coventry, U.K., as a visiting research student.

Wei Hua (SM'16) received B.Sc. and Ph.D. degrees in electrical engineering from the School of Electrical Engineering, Southeast University, Nanjing, China, in 2001 and 2007, respectively.

Since 2007, he has been with Southeast University, where he is currently a Chair Professor in the School of Electrical Engineering. He has authored and co-authored over 140 technical papers, and he is the holder of 60 patents in his areas of interest. His teaching and research interests include the design, analysis, and control of electrical machines.

Ming Cheng (M'01–SM'02–F'15) received the B.Sc. and M.Sc. degrees in electrical engineering from Southeast University, Nanjing, China, in 1982 and 1987, respectively, and the Ph.D. degree in electrical and electronic engineering from the University of Hong Kong, Hong Kong, in 2001.

Since 1987, he has been with Southeast University, where he is currently a Chair Professor in the School of Electrical Engineering and the Director of the Research Center for Wind Power Generation. From January to April 2011, he was a Visiting Professor at the Wisconsin Electric Machine and Power Electronics Consortium, University of Wisconsin, Madison, WI, USA. He has authored or co-authored more than 400 technical papers and 5 books, and is the holder of 130 patents in his research areas. His teaching and research interests include electrical machines, motor drives for electric vehicles, and renewable energy generation.

Prof. Cheng is a fellow of the Institution of Engineering and Technology. He has served as the Chair and Organizing Committee Member for many international conferences. He was a Distinguished Lecturer of the IEEE Industry Applications Society in 2015/2016.

Juliette Soulard (M'00) received her Ph.D. degree in electrical engineering from the University of Paris VI, France, in 1998. From 1999 to 2016, she led research on electric machines for industrial applications at the KTH Royal Institute of Technology, Stockholm, Sweden, in close collaboration with the Swedish industry. Since 2016, she has been an Associate Professor with the Warwick Manufacturing Group, University of Warwick, Coventry, United Kingdom.

Her current research activities are focused on accounting for manufacturing effects in modeling and design of permanent-magnet synchronous machines used in advanced propulsion systems.
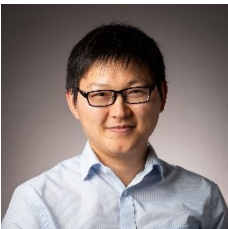
Z. Q. Zhu (M'90–SM'00–F'09) received the B.Eng. and M.Sc. degrees in electrical and electronic engineering from Zhejiang University, Hangzhou, China, in 1982 and 1984, respectively, and the Ph.D. degree in electrical and electronic engineering from The University of Sheffield, Sheffield, U.K., in 1991.

Since 1988, he has been with The University of Sheffield, where he is currently a Research Chair of the Royal Academy of Engineering/Siemens with the Department of Electronic and Electrical Engineering and the Head of the Electrical Machines and Drives Research Group. His current research interests include the design and control of permanent-magnet brushless machines and drives for applications ranging from automotive through domestic appliances to renewable energy.

Dr. Zhu is a Fellow of the Royal Academy of Engineering.

Zhongze Wu (M'18) received the B.Eng. and M.Sc. degrees in electrical engineering from Southeast University, Nanjing, China, in 2010 and 2013, respectively, and the Ph.D. degree in electrical and electronic engineering from The University of Sheffield, Sheffield, U.K., in January 2017.

Since August 2018, he has been with the Institute for Advanced Automotive Propulsion Systems (IAAPS), Department of Mechanical Engineering, University of Bath, Bath, U.K., where he is currently a Prize Fellow in Electric Propulsion. His major research interests include the advanced electrical machines and drives for electric propulsion systems.

From January 2017 to August 2018, he was with the Warwick Manufacturing Group (WMG), University of Warwick, Coventry, U.K., as a research fellow in electrical machines.